catalysts

MDPI

Article

Carbon Nanofiber-Encapsulated FeCoNiCuMn Sulfides with Tunable S Doping for Enhanced Oxygen Evolution Reaction

Yuhan Sun [1,†], Chen Shen [2,†], Mingran Wang [1], Yang Cao [1], Qianwei Wang [1], Jiayi Rong [1], Tong He [3,*], Duanyang Li [4,*] and Feng Cao [1,*]

[1] Key Lab for Anisotropy and Texture of Materials (MoE), School of Materials Science and Engineering, Northeastern University, Shenyang 110819, China; 2170505@stu.neu.edu.cn (Y.S.); 2200639@stu.neu.edu.cn (M.W.); 2270359@stu.neu.edu.cn (Y.C.); 2270554@stu.neu.edu.cn (Q.W.); 2210214@stu.neu.edu.cn (J.R.)
[2] Key Laboratory of Renewable Energy, Guangzhou Institute of Energy Conversion, Chinese Academy of Sciences, Guangzhou 510640, China; shenchen@ms.giec.ac.cn
[3] Analytical Testing Center, Northeastern University, Shenyang 110819, China
[4] College of Mechanical Engineering, Shenyang University, Shenyang 110003, China
* Correspondence: tonghe503@126.com (T.H.); dyli@alum.imr.ac.cn (D.L.); caof@atm.neu.edu.cn (F.C.)
† These authors contributed equally to this work.

Abstract: The oxygen evolution reaction (OER) stands out as a key electrochemical process for the conversion of clean energy. However, the practical implementation of OER is frequently impeded by its slow kinetics and the necessity for scarce and expensive noble metal catalysts. High-entropy transition metal sulfides (HETMS) stand at the forefront of OER catalysts, renowned for their exceptional catalytic performance and diversity. Herein, we have synthesized a HETMS catalyst, $(FeCoNiCuMn_{50})S_2$, encapsulated within carbon nanofibers through a one-step process involving the synergistic application of electrospinning and chemical vapor deposition. By precisely controlling the doping levels of sulfur, we have demonstrated that sulfur incorporation significantly increases the exposed surface area of alloy particles on carbon nanofibers and optimizes the electronic configuration of the alloy elements. These findings reveal that sulfur doping is instrumental in the substantial improvement of the catalyst's OER performance. Notably, the catalyst showed optimal activity at a sulfur-to-metal atom ratio of 2:1, delivering an overpotential of 254 mV at a current density of 10 mA cm^{-2} in 1.0 M KOH solution. Furthermore, the $(FeCoNiCuMn_{50})S_2$ catalyst exhibited remarkable electrochemical stability, underscoring its potential as an efficient and robust OER electrocatalyst for sustainable energy applications.

Keywords: high-entropy transition metal sulfides; oxygen evolution reaction; electrospinning; carbon nanofibers

check for updates

Citation: Sun, Y.; Shen, C.; Wang, M.; Cao, Y.; Wang, Q.; Rong, J.; He, T.; Li, D.; Cao, F. Carbon Nanofiber-Encapsulated FeCoNiCuMn Sulfides with Tunable S Doping for Enhanced Oxygen Evolution Reaction. *Catalysts* **2024**, *14*, 626. https://doi.org/10.3390/catal14090626

Academic Editor: Carlo Santoro

Received: 29 August 2024
Revised: 12 September 2024
Accepted: 14 September 2024
Published: 17 September 2024

Copyright: © 2024 by the authors. Licensee MDPI, Basel, Switzerland. This article is an open access article distributed under the terms and conditions of the Creative Commons Attribution (CC BY) license (https://creativecommons.org/licenses/by/4.0/).

1. Introduction

In recent years, the pursuit of clean and sustainable energy through water electrolysis has gained considerable momentum as a key research focus [1–5]. A crucial element of this process is the Oxygen Evolution Reaction (OER), which drives the anodic generation of oxygen from water—a step that significantly influences the overall efficiency of electrolytic systems [6–10]. Historically, the effectiveness of the OER has been attributed to noble metal-based catalysts, particularly RuO_2 and IrO_2, which are well regarded for their superior catalytic performance [11,12]. However, the limited availability, high cost, and challenging extraction processes associated with these metals have severely restricted their widespread industrial adoption [13–15]. Consequently, the imperative to develop oxygen evolution reaction (OER) catalysts that are economically feasible, yet maintain high catalytic efficiency and chemical stability, is more critical than ever. As the field of electrocatalysis advances, ongoing research is not only deepening our fundamental comprehension of these processes but also laying a robust groundwork for the next generation

of energy conversion technologies. This pursuit of efficient, durable, and economically accessible OER catalysts is a driving force in material science and electrochemistry, holding the promise of a more sustainable and eco-friendly energy future [16–20]. Strenuous efforts have been devoted to develop nonprecious metal-based catalysts. Among the potential alternatives, transition metal sulfides (TMSs), along with phosphides, nitrides, and carbides, have emerged as promising candidates for electrocatalysts due to their cost-effectiveness and outstanding catalytic properties, with the potential to surpass traditional noble metal oxide catalysts [21–23]. Among these, TMSs have attracted considerable attention owing to their unique structural advantages, abundant active sites, and tunable electronic properties [24–26]. Combining TMSs with carbon substrate is a traditional method to obtain high catalytic activity. The carbon matrix not only serves as a support material to prevent the aggregation or dissolution of metal nanoparticles (NPs) under harsh operating conditions but also serves as an active site to enhance catalytic performance [26]. However, monometallic sulfides are limited by their single-metal composition, which often results in suboptimal catalytic activity and stability. Enhancing the performance of these materials remains a challenging and important area of research. HETMS represent an innovative class of materials derived from the strategic combination of high-entropy alloys (HEAs) with metal sulfides. The complex electronic and lattice structures of high-entropy alloys may endow them with unique catalytic properties [27–29]. This integration exploits the synergistic effects of multiple metal elements with sulfur, leading to enhanced electron transfer kinetics and an expanded array of active sites [30–32]. These intrinsic properties are crucial for significantly improving the catalytic performance of materials, particularly in the context of the OER [33,34]. For example, Zhao et al. [35] successfully synthesized an FeCoNiCuAlV sulfide that demonstrated an overpotential of 362 mV at 20 mA cm^{-2} for the OER in 1 M KOH solution, with a Tafel slope of 120 mV dec^{-1}, highlighting its promising catalytic properties. Despite the progress in HETMS research, the synthesis methodologies typically require sophisticated equipment and intricate processes. Additionally, phase separation into microdomains rather than the formation of a homogeneous solid solution is often observed, posing a significant challenge in the development of straightforward synthesis approaches that can achieve uniform elemental distribution and superior catalytic performance.

Herein, we successfully fabricated carbon nanofiber-coated high-entropy transition metal sulfides, designated as $(FeCoNiCuMn_{50})S_x$, with precisely controlled sulfur doping levels. This was achieved through a synergistic combination of electrospinning and chemical vapor deposition techniques. A systematic evaluation of these materials for the OER demonstrated that $(FeCoNiCuMn_{50})S_2$ outperformed the other variants, achieving an overpotential of 254 mV at a current density of 10 mA cm^{-2} in N_2-saturated 1.0 M KOH solution. The catalyst's performance reached its peak at an optimal sulfur-to-metal atomic ratio of 2:1, beyond which a decline was observed, indicating a bell-shaped dependency on sulfur content. The superior OER activity of $(FeCoNiCuMn_{50})S_2$ is attributed to the formation of nanoparticles on the carbon nanofibers during the sulfidation process, which enhanced the active surface area, as well as the electronic restructuring within the alloy. Additionally, the catalyst exhibited remarkable electrochemical stability over extended periods. These characteristics position $(FeCoNiCuMn_{50})S_2$ as a highly promising OER electrocatalyst, with significant potential to advance energy conversion and storage technologies.

2. Result and Discussion

2.1. Characterizations of Samples

For the synthesis of high-entropy metal transition sulfide nanoparticles, referred to as $HETMS_2$, a series of $FeCoNiCuMn_x$@CNFs (where x represents Mn content at 10, 30, 50, 80, and 100%) were fabricated via electrospinning followed by high-temperature carbonization, as illustrated in Figure 1a. Among these, the high-entropy alloy nanocrystals with an optimal Mn content of 50, denoted as $FeCoNiCuMn_{50}$@CNFs (Figure S1), exhibited the most promising OER performance and were subsequently selected for further sulfidation, resulting in a range of $HETMS_x$ materials with varying sulfur contents. Using Scanning Electron Microscopy (SEM), a preliminary investigation of the microstructure of the

$(FeCoNiCuMn_{50})S_2$ catalyst was conducted, revealing that after sulfidation, the nanofibers have a diameter of 120 nm (Figure 1b), with metallic sulfide particles uniformly dispersed along the carbon nanofibers, with particle sizes of approximately 14 nm (Figure 1b). SEM images before and after sulfidation (Figure S2) show that the alloy particles protrude from the surface of the nanofibers after sulfidation, indicating an increase in active surface area. Further characterization with Transmission Electron Microscopy (TEM) provided detailed insights into the lattice parameters, with the interplanar spacing measured at 0.305 nm, representing a slight expansion relative to the standard 0.302 nm spacing for the (111) plane of a cubic crystal (Figure 1b). This expansion is attributed to the formation of a multi-component alloy, a signature characteristic of high-entropy materials, which is believed to enhance the catalytic performance in the oxygen evolution reaction [31]. X-ray Diffraction (XRD) analysis of the $(FeCoNiCuMn_{50})S_x$ nanoparticles confirmed the presence of an FCC phase, indexed as PDF#06-0518. Distinct diffraction peaks corresponding to the (111), (200), (220), (311), (222), (400), and (420) planes were observed at 2θ values of 29.6°, 34.3°, 49.3°, 58.6°, 61.4°, 72.3°, and 82.5°, respectively [36]. An additional peak at 25° was attributed to the (002) plane of graphite carbon [37], as shown in Figure 1f. Energy-Dispersive X-ray Spectroscopy (EDS) analysis, detailed in Table S1, confirmed that the sulfur-to-metal elemental ratio closely matched the targeted stoichiometry of MS_x, where x equals 0.5, 1, 2, or 4. These results collectively validate the successful synthesis of HETMS materials with the desired $(FeCoNiCuMn_{50})S_x$ chemical composition.

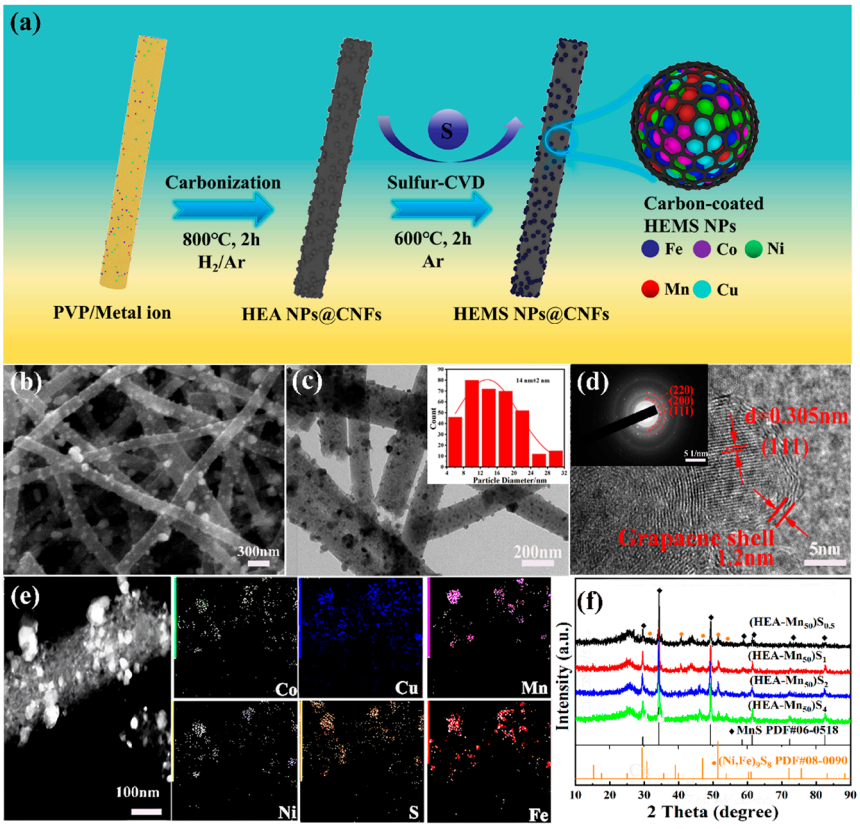


Figure 1. Characterization of high-entropy metal sulfide $(FeCoNiCuMn_{50})S_2$ nanoparticles. (**a**) Schematic of the synthesis process; (**b**) SEM image; (**c**) TEM image and particle size distribution (inset); (**d**) HRTEM image and SAED image (inset); (**e**) STEM and corresponding mapping images; and (**f**) XRD of $(FeCoNiCuMn_{50})S_x$.

X-ray Photoelectron Spectroscopy (XPS) was utilized to examine the chemical states of elements in high-entropy metal sulfide $(FeCoNiCuMn_{50})S_2$ before and after sulfidation. As shown in Figure S3, prior to sulfidation, an increase in Mn content resulted in a shift of photoelectron peak positions for Fe, Co, Ni, and Cu to higher binding energies, indicative

of reduced electron density around these metals. Conversely, the Mn $2p_{3/2}$ peak shifted to a lower binding energy at 642.1 eV, suggesting an electron-rich state, which may facilitate a synergistic effect among the metal atoms, beneficial for the OER [38]. Post-sulfidation, the XPS spectra revealed peaks corresponding to higher oxidation states for all metal elements in $(FeCoNiCuMn_{50})S_2$ (Figure 2). The initial peaks for the metallic states were replaced by those for Fe^{3+} at 711.0 eV and 724.6 eV (Figure 2a), Co^{3+} at 777.9 eV and 794.3 eV (Figure 2b), Ni^{3+} at 855.9 eV and 878.6 eV (Figure 2c), and Cu^{+} at 932.4 eV and 946.0 eV (Figure 2d), respectively. As shown in Figure 2e, the Mn 2p peak was deconvoluted into components at 641.2 eV (Mn^{2+} $2p_{3/2}$), 642.7 eV (Mn^{3+} $2p_{3/2}$), 644.7 eV, and 648.2 eV (Mn^{4+} $2p_{3/2}$) [39–43]. The S 2p XPS results (Figure 2f) confirmed the formation of chemical bonds between sulfur and both metal elements and carbon, indicating successful sulfur incorporation into the carbon nanofibers and its interaction with carbon [44]. These findings collectively suggest that the material undergoes a transformation from a metallic alloy to a sulfide compound, a change that is likely to enhance its OER performance.

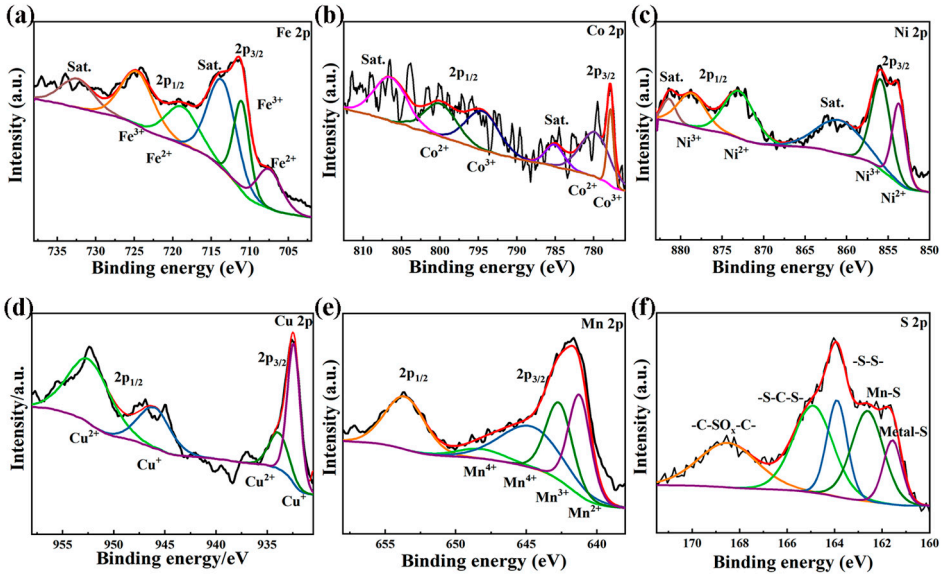


Figure 2. XPS spectra of (**a**) Fe 2p; (**b**) Co 2p; (**c**) Ni 2p; (**d**) Cu 2p; (**e**) Mn 2p; and (**f**) S 2p of np-HETMS $(FeCoNiCuMn_{50})S_2$ nanoparticles.

2.2. Electrocatalytic Performance on OER for Different Samples

The OER electrocatalytic performance of the synthesized high-entropy metal sulfides was evaluated using a conventional three-electrode system in an N_2-saturated 1.0 M KOH solution. Linear sweep voltammetry (LSV) was employed to assess the catalytic activity, with the working electrode (WE) composed of catalyst-loaded carbon paper. A mercury/mercury oxide (Hg/HgO) electrode served as the reference, while graphite rods were utilized as the counter electrodes. The LSV polarization curves, shown in Figure 3a, reveal that the $(FeCoNiCuMn_{50})S_2$ catalyst exhibits an overpotential of 254 mV at a current density of 10 mA cm^{-2}, surpassing its counterparts with varying sulfur content, specifically $(FeCoNiCuMn_{50})S_{0.5}$ at 315 mV, $(FeCoNiCuMn_{50})S_1$ at 302 mV, and $(FeCoNiCuMn_{50})S_4$ at 285 mV. This result indicates that the optimal sulfur-to-metal atomic ratio for the $(FeCoNiCuMn_{50})S_2$ catalyst is 2:1. As the sulfur content increases, the overpotential at a current density of 10 mA cm^{-2} follows a trend of initial reduction, reaching a minimum at the optimal ratio, followed by an increase at higher sulfur levels. This behavior can be attributed to the increased sulfur content, which introduces a higher number of lattice defects and enhances synergistic effects. These modifications effectively lower the energy barrier between intermediate species O* and OOH*, optimizing their adsorption and desorption energies on the catalyst surface, thereby improving OER performance [45]. However, an excessively high sulfur content can lead to the fracture of carbon nanofibers,

resulting in a decline in the catalytic performance of the alloy, as illustrated in Figure S4. Moreover, the $(FeCoNiCuMn_{50})S_2$ catalyst demonstrated superior activity compared with the industrial benchmark catalyst RuO_2, which exhibited an overpotential of 277 mV under the same conditions. The superior performance of $(FeCoNiCuMn_{50})S_2$ was further corroborated by its Tafel slope, derived from the LSV data. With a Tafel slope of 74 mV dec^{-1}, as shown in Figure 3b, the catalyst demonstrates faster reaction kinetics than the other samples, consistent with its excellent LSV performance. Additionally, the activity of the $(FeCoNiCuMn_{50})S_2$ catalyst surpasses that of several recently reported OER catalysts, as depicted in Figure 3c, highlighting its remarkable catalytic potential.

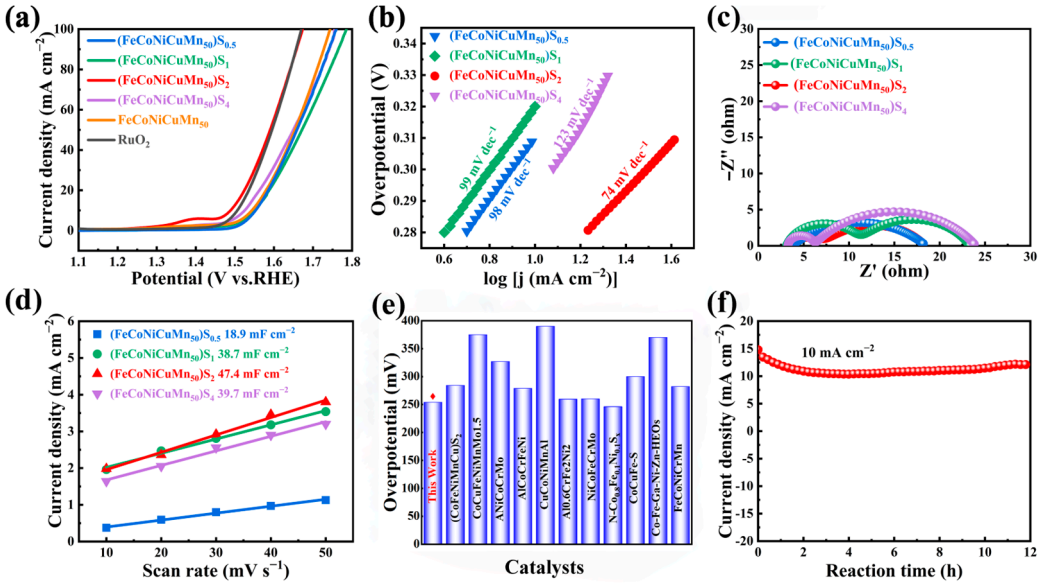


Figure 3. Electrocatalytic performance of different samples. (**a**) OER polarization curves of different samples. (**b**) Tafel plots. (**c**) Nyquist plots for different samples. (**d**) Capacitive currents as a function of scan rate. (**e**) Performance diagram of OER electrocatalysts. (**f**) Stability testing.

To elucidate the disparities in catalytic performance among the catalysts, a comprehensive analysis of the electrochemical active surface area (ECSA) and charge transfer resistance was conducted for the various samples. The findings, as presented in Figure 3d, reveal that $(FeCoNiCuMn_{50})S_2$ exhibits the highest double-layer capacitance at 47.4 mF cm^{-2}, surpassing that of $(FeCoNiCuMn_{50})S_4$, $(FeCoNiCuMn_{50})S_1$, and $(FeCoNiCuMn_{50})S_{0.5}$, which have values of 39.7 mF cm^{-2}, 38.7 mF cm^{-2}, and 18.9 mF cm^{-2}, respectively. This enhanced capacitance indicates an increased number of active sites [46]. Based on these results, the calculated ECSA values were utilized to replace the geometric surface area, thereby deriving the relationship curve between the current density and potential of the electrocatalyst. As shown in Figure S7, compared with other samples, $(FeCoNiCuMn_{50})S_2$ demonstrated superior performance in terms of maximum current density, suggesting that its intrinsic activity has been enhanced and its catalytic performance improved. Figure 3e further illustrates that $(FeCoNiCuMn_{50})S_2$ also exhibits the lowest charge transfer resistance, consistent with its superior OER activity.

The exceptional catalytic performance of the high-entropy metal sulfide $(FeCoNiCuMn_{50})S_2$ can be attributed to two key factors. Firstly, the gradual outward growth of nanoparticles on the carbon nanofibers during the sulfidation process effectively increases the active surface area, which is critical in enhancing catalytic activity. Notably, normalization of the ECSA reveals that $(FeCoNiCuMn_{50})S_2$ still exhibits the highest intrinsic activity. This observation indicates that the enhancement in the sample's catalytic performance is not solely attributed to the increase in specific surface area. Secondly, the synergistic interactions among the alloy components, coupled with the electronic structural modifications subsequent to sulfidation, play a vital role in the material's performance. The XPS results, as previously discussed, reveal that Mn^{2+} acts as an

electron acceptor, while Fe, Co, Ni, and Cu serve as electron donors [47,48]. This electron transfer dynamic facilitates the attainment of a high-valence state for the metal ions after sulfidation, promoting the accelerated desorption of reaction intermediates. These synergistic effects are pivotal in significantly enhancing the OER performance [24].

The long-term stability of a catalyst, akin to its catalytic rate, is a critical parameter for industrial viability. The durability of the $(FeCoNiCuMn_{50})S_2$ catalyst was assessed through the application of a constant potential of 0.6 V (1.484 V vs. RHE) over a period of 12 h in 1.0 M KOH. Figure 3f displays the results, which demonstrate that the material's current density is sustained at 10 mA cm^{-2} for the entire duration, with only a minor decrease and subsequent stabilization, indicative of its commendable electrochemical stability. Furthermore, the sample's morphological evolution throughout the OER process was scrutinized via TEM (Figure S8). The TEM imagery distinctly demonstrates that, post the stability testing, the $(FeCoNiCuMn_{50})S_2$ particles avoided aggregation, retained dimensions of about 14 nm, exhibited an unaltered lattice spacing, and displayed a uniform distribution of metallic elements, all of which corroborate the absence of phase separation throughout the catalytic reaction. This remarkable stability is attributed to the material's high-entropy structure [49] and the protective carbon encapsulation [50], which together underpin its potential for industrial-scale applications.

3. Materials and Methods

3.1. Materials

Nickel nitrate hexahydrate ($Ni(NO_3)_2{\cdot}6H_2O$), cobalt nitrate hexahydrate ($Co(NO_3)_2{\cdot}6H_2O$), iron nitrate nonahydrate ($Fe(NO_3)_3{\cdot}9H_2O$), copper nitrate trihydrate ($Cu(NO_3)_3{\cdot}3H_2O$), chromium nitrate nonahydrate ($Cr(NO_3)_3{\cdot}9H_2O$), manganese nitrate tetrahydrate ($Mn(NO_3)_2{\cdot}4H_2O$), polyvinyl pyrrolidone (PVP, $(C_6H_9NO)_n$), Sulfur (S) and N,N-Dimethylformamide (C_3H_7NO) were purchased from Sinopharm Chemical Reagent Co., Ltd. Shanghai, China. Potassium chloride (KCl) and potassium hydroxide (KOH) were purchased from Yongda Chemical Reagent Co., Ltd., Tianjin, China. The Nafion solution was purchased from Minnesota Minerals and Manufacturing Company, Saint Paul, MN, USA. All chemical reagents are of analytical grade ($\geq$99.7%) and no further purification is required.

3.2. Materials Synthesis

Initially, the fabrication process commenced with the synthesis of a spinning solution, wherein a metal precursor was homogeneously mixed with polyvinylpyrrolidone (PVP K-10, 5.5 g) in dimethylformamide (DMF, 10 mL) at ambient temperature under constant stirring for a duration of 12 h. This solution was subsequently electrospun to yield nanofibers, which were subjected to carbonization within an H_2/Ar atmosphere, facilitating the formation of high-entropy alloy nanoparticles encapsulated within a carbon matrix along the nanofibers. To generate samples with diverse compositions, the ratio of manganese salts in the spinning solution was meticulously adjusted.

Proceeding to the sulfurization stage, a mixture of $FeCoNiCuMn_{50}$@CNFs and sublimed sulfur was loaded into a tube furnace under an argon atmosphere. The temperature was incrementally elevated from room temperature to 60 °C at a controlled rate of 5 °C per minute, where it was maintained for a period of 2 h prior to natural cooling. At this elevated temperature, the sublimed sulfur powder transformed into gaseous sulfur (S), which interacted comprehensively with the high-entropy alloy nanocrystals to yield high-entropy metal sulfides ($HETMS_x$) during the annealing process. The sulfur content within the resulting $HETMS_x$ was meticulously regulated by varying the mass ratio of sublimed sulfur to $FeCoNiCuMn_{50}$@CNFs, with ratios of 0.5, 1, 2, and 4 employed to produce a series of $HETMS_x$ with distinct sulfur concentrations.

3.3. Material Characterization

Powder X-ray diffraction (XRD) measurements were performed on a Rigaku SmartLab X-ray diffractometer (using Cu Kα radiation). The SmartLab X-ray diffractometer is produced by Rigaku Corporation, based in Tokyo, Japan. Microscopic morphology

testing was conducted using a JEM-2100F transmission electron microscope (TEM) and a JSM-7001F scanning electron microscope (SEM) equipped with an energy-dispersive X-ray (EDX) spectrometer, both operated at 15 kV, JEM-2100F and JSM-7001F, are manufactured by JEOL Ltd., which is based in Tokyo, Japan. Additionally, surface chemical analysis was performed using X-ray photoelectron spectroscopy (XPS) on an Escalab 250Xi system, manufactured by Thermo Fisher Scientific, which is based in Waltham, Massachusetts, United States.

3.4. Electrochemical Measurements

All electrochemical measurements were carried out using a three-electrode system equipped with a CHI1960 electrochemical workstation. Hg/HgO electrode was used as the reference electrode, and a graphite rod served as the counter electrode. For each measurement, 5 mg of sample and 10 μL of a 5 wt% Nafion solution were added to a 0.8 mL water/ethanol mixture in a 3:1 volume ratio and sonicated for 30 min to form a homogeneous ink. Then, 30 μL of this ink was carefully dropped onto a carbon paper with an area of 1 × 1.5 cm^2 for 5 times and dried in air. Linear sweep voltammetry (LSV) polarization curves were recorded in a 1 M KOH solution with a scan rate of 5 mV s^{-1} and a scan range of 0.1–1.1 V. The Tafel slope was calculated from the LSV polarization curve according to the equation as follow:

$$\eta = a + b \log j$$

where j was the current density, b was the Tafel slope, η was the overpotential.

Cyclic voltammograms (CVs) at various scan rates (10, 20, 30, 40, 50 mV/s) were collected in the 0.15–0.2 V vs. RHE range. Double-layer capacitance (C_{dl}) can be estimated by CV measures. The electrochemical surface area (ECSA) was assessed from the electrochemical double-layer capacitance (C_{dl}). The electrochemical impedance spectroscopy (EIS) measurements were carried out at a potential of 1.555 V vs. RHE with frequencies of 0.1 Hz to 100,000 Hz and an amplitude of 5 mV. An equivalent Randles circuit model was fit to the data to determine the system resistance and capacitance.

4. Conclusions

The synthesis of $(FeCoNiCuMn_{50})S_2$ high-entropy metal sulfide as an OER catalyst has been successfully achieved through a combination of electrospinning and chemical deposition techniques. Our research underscores the profound influence of sulfur content on catalytic activity, identifying an optimal sulfur-to-metal atomic ratio of 2:1. The gradual outward growth of nanoparticles on the carbon nanofibers during the sulfidation process, coupled with the synergistic interactions among the alloy components, endows the $(FeCoNiCuMn_{50})S_2$ electrode with exceptional OER catalytic activity. Notably, this material facilitates a current density of 10 mA cm^{-2} at a remarkably low overpotential of 254 mV. Moreover, the $(FeCoNiCuMn_{50})S_2$ electrode has demonstrated sustained stability over a 12 h period at a current density of 10 mA cm^{-2}. Collectively, these findings highlight the potential of $(FeCoNiCuMn_{50})S_2$ as an efficient, stable, and promising OER electrocatalyst.

Supplementary Materials: The following are available online at https://www.mdpi.com/article/10.3390/catal14090626/s1, Figure S1. LSV curves of $FeCoNiCuMn_x$ with varying Mn content. Figure S2. SEM images of $FeCoNiCuMn_x$@CNFs. (a) X = 10; (b) X = 30; (c) X = 50; (d) X = 70; (e) X = 100. Figure S3. XPS spectra of $FeCoNiCuMn_{10}$@CNFs and $FeCoNiCuMn_{50}$@CNFs. (a) Survey; (b) Fe 2p; (c) Co 2p; (d) Ni 2p; (e) Cu 2p; (f) Mn 3d. Figure S4. SEM images of $(FeCoNiCuMn_{50})S_x$ with sulfur content S = 0.5, 1, 4. Figure S5. Equivalent circuit model of $(FeCoNiCuMn_{50})S_x$. Figure S6. CV of $(FeCoNiCuMn_{50})S_x$ with sulfur content S = 0.5, 1, 4, 2. Figure S7. Specific current density driven from calculated ECSA versus potential. Figure S8. Stability tests of catalysts: (a) TEM, (b) HRTEM, and (c) elemental maps. Table S1. EDS results of $(FeCoNiCuMn_{50})S_x$.

Author Contributions: Y.S. and C.S.: Conceptualization, methodology, investigation, and writing–original draft; M.W., Y.C., Q.W., and J.R.: Investigation, data curation, and formal analysis; T.H., D.L.,

and F.C.: Formal analysis, writing–review and editing, supervision, and funding acquisition. All authors have read and agreed to the published version of the manuscript.

Funding: This research was funded by the National Natural Science Foundation of China (51971059 and 52371150), and the Natural Science Foundation of Liaoning Province of China (2023-MS-070 and 2022-MS-293).

Data Availability Statement: All data generated of this work are included in this article.

Acknowledgments: Special thanks are due to the Analytical and Testing Center, Northeastern University, for the instrumental and data analysis.

Conflicts of Interest: The authors declare no conflicts of interest.

References

1. Wang, Y.; Xu, Z.; Wu, X.; Wu, Z.-S. Recent advances and key perspectives of in-situ studies for oxygen evolution reaction in water electrolysis. *Green Energy Environ.* **2023**, *9*, 1497–1517. [CrossRef]
2. Wang, S.; Geng, Z.; Bi, S.; Wang, Y.; Gao, Z.; Jin, L.; Zhang, C. Recent advances and future prospects on Ni3S2-Based electrocatalysts for efficient alkaline water electrolysis. *Green Energy Environ.* **2024**, *9*, 659–683. [CrossRef]
3. Bernt, M.; Hartig Weiß, A.; Tovini, M.F.; El-Sayed, H.A.; Schramm, C.; Schröter, J.; Gebauer, C.; Gasteiger, H.A. Current Challenges in Catalyst Development for PEM Water Electrolyzers. *Chem. Ing. Tech.* **2019**, *92*, 31–39. [CrossRef]
4. Tang, J.; Xu, X.; Tang, T.; Zhong, Y.; Shao, Z. Perovskite-Based Electrocatalysts for Cost-Effective Ultrahigh-Current-Density Water Splitting in Anion Exchange Membrane Electrolyzer Cell. *Small Methods* **2022**, *6*, 2201099.
5. Yang, L.; Shi, L.; Chen, H.; Liang, X.; Tian, B.; Zhang, K.; Zou, Y.; Zou, X. A Highly Active, Long-Lived Oxygen Evolution Electrocatalyst Derived from Open-Framework Iridates. *Adv. Mater.* **2023**, *35*, 2208539.
6. Xie, X.; Du, L.; Yan, L.; Park, S.; Qiu, Y.; Sokolowski, J.; Wang, W.; Shao, Y. Oxygen Evolution Reaction in Alkaline Environment: Material Challenges and Solutions. *Adv. Funct. Mater.* **2022**, *32*, 2110036. [CrossRef]
7. Huang, H.; Xue, Y.; Xie, Y.; Yang, Y.; Yang, L.; He, H.; Jiang, Q.; Ying, G. MoS_2 quantum dot-decorated MXene nanosheets as efficient hydrogen evolution electrocatalysts. *Inorg. Chem. Front.* **2022**, *9*, 1171–1178. [CrossRef]
8. Chen, Z.; Han, G.-F.; Mahmood, A.; Hou, J.; Wei, W.; Shon, H.K.; Wang, G.; Waite, T.D.; Baek, J.-B.; Ni, B.-J. Mechanosynthesized electroactive materials for sustainable energy and environmental applications: A critical review. *Prog. Mater. Sci.* **2024**, *145*, 101299. [CrossRef]
9. Wang, N.; Ji, L.; Zhai, Y. WO3-Xas An Activation Medium to Prompt Overall Water Splitting of Nife-Based Electrocatalyst. *J. Colloid Interf. Sci.* **2024**, *669*, 53–63.
10. Deng, X.; Chen, J.; Chen, Q.; Zhou, Y.; Liu, X.; Zhang, J.; Wang, G.; Wang, R. The synergistic effect of Ir and oxygen vacancies on Enhancing the OER performance of Surface-Reconstructed FeCo LDH. *Appl. Surf. Sci.* **2024**, *665*, 160310. [CrossRef]
11. Zhu, Y.; Klingenhof, M.; Gao, C.; Koketsu, T.; Weiser, G.; Pi, Y.; Liu, S.; Sui, L.; Hou, J.; Li, J.; et al. Facilitating alkaline hydrogen evolution reaction on the hetero-interfaced Ru/RuO2 through Pt single atoms doping. *Nat. Commun.* **2024**, *15*, 1447. [CrossRef] [PubMed]
12. da Silva, G.C.; Fernandes, M.R.; Ticianelli, E.A. Activity and Stability of Pt/IrO_2 Bifunctional Materials as Catalysts for the Oxygen Evolution/Reduction Reactions. *ACS Catal.* **2018**, *8*, 2081–2092. [CrossRef]
13. Devendrachari, M.C.; Palem, R.R.; Shimoga, G.; Kim, S.Y.; Choi, D.S. Enhanced oxygen evolution reaction by controlled assembly of Co3O4 nanorods on TiB2 nanosheets. *Surf. Interfaces* **2024**, *51*, 104619.
14. Fu, G.; Cui, Z.; Chen, Y.; Xu, L.; Tang, Y.; Goodenough, J.B. Hierarchically mesoporous nickel-iron nitride as a cost-efficient and highly durable electrocatalyst for Zn-air battery. *Nano Energy* **2017**, *39*, 77–85. [CrossRef]
15. Liu, Z.J.; Zhao, Z.H.; Wang, Y.Y.; Dou, S.; Yan, D.F.; Liu, D.D.; Xia, Z.H.; Wang, S.Y. In Situ Exfoliated, Edge-Rich, OxygenFunctionalized Graphene from Carbon Fibers for Oxygen Electrocatalysis. *Adv. Mater.* **2017**, *29*, 1606207.
16. Pan, S.; Ma, Z.; Yang, Z.; Dongyang, B.; Yang, H.; Lai, S.; Dong, F.; Yang, X.; Lin, Z. Magnesium incorporation activates perovskite cobaltites toward efficient and stable electrocatalytic oxygen evolution. *Mater. Rep. Energy* **2023**, *3*, 100212.
17. Abdelghafar, F.; Xu, X.; Guan, D.; Lin, Z.; Hu, Z.; Ni, M.; Huang, H.; Bhatelia, T.; Ping, S.; Shao, J. New Nanocomposites Derived from Cation-Nonstoichiometric Bax(Co, Fe, Zr, Y)O3−δ as Efficient Electrocatalysts for Water Oxidation in Alkaline Solution. *ACS Mater. Lett.* **2024**, *6*, 2985–2994.
18. Zhang, W.; Zhao, Y.; Xu, J.; Jia, B.; Zhang, W.; Qin, M. Guided Design of Efficient Oxygen Evolution Catalysts Using Patent Analysis. *ACS Omega* **2024**, *9*, 18160–18168.
19. Yuan, C.Z.; Zhao, H.; Huang, S.; Li, J.; Zhang, L.; Zhao, W.; Weng, Y.; Zhang, X.; Ye, S.; Chen, Y. Designing and regulating catalysts for enhanced oxygen evolution in acid electrolytes. *Carbon Neutralization* **2023**, *2*, 467–493.
20. Wei, X.; Cao, S.; Cheng, S.; Lu, C.; Chen, X.; Lu, X.; Chen, X.; Dai, F. Unraveling the Intrinsic Mechanism of High-Performance Two-Dimensional Conjugated Metal–Organic Frameworks for ORR/OER through Theoretical Investigation. *ACS Mater. Lett.* **2024**, *6*, 3496–3504.
21. Shi, Y.; Zhu, B.; Guo, X.; Li, W.; Ma, W.; Wu, X.; Pang, H. MOF-derived metal sulfides for electrochemical energy applications. *Energy Storage Mater.* **2022**, *51*, 840–872. [CrossRef]

22. Guo, Y.; Park, T.; Yi, J.W.; Henzie, J.; Kim, J.; Wang, Z.; Jiang, B.; Bando, Y.; Sugahara, Y.; Tang, J.; et al. Nanoarchitectonics for transition-metal-sulfide-based electrocatalysts for water splitting. *Adv. Mater.* **2019**, *31*, e1807134. [PubMed]
23. Zheng, X.; Cao, Y.; Wu, Z.; Ding, W.; Xue, T.; Wang, J.; Chen, Z.; Han, X.; Deng, Y.; Hu, W. Rational design and spontaneous sulfurization of NiCo-(oxy) hydroxysulfides nanosheets with modulated local electronic configuration for enhancing oxygen electrocatalysis. *Adv. Energy Mater.* **2022**, *12*, 2103275.
24. Sari, F.N.I.; Lai, Y.; Huang, Y.; Wei, X.; Pourzolfaghar, H.; Chang, Y.; Ghufron, M.; Li, Y.; Su, Y.; Clemens, O.; et al. Electronic Structure Engineering in NiFe Sulfide via A Third Metal Doping as Efficient Bifunctional OER/ORR Electrocatalyst for Rechargeable Zinc-Air Battery. *Adv. Funct. Mater.* **2024**, *34*, 2310181. [CrossRef]
25. Wang, J.; Wu, Y.; Yu, H.; Hang, C.; Tang, W.; Yang, Y.; Chen, H.; Li, H.; Yu, F. Three-dimensional pine-tree-like bimetallic sulfide with maximally exposed active sites by secondary structural restructuring for efficient electrocatalytic OER. *Int. J. Hydrogen Energy* **2024**, *79*, 1418–1426. [CrossRef]
26. Viswanathan, S.S. Nanocarbons-Based Trifunctional Electrocatalysts for Overall Water Splitting and Metal-Air Batteries: Metal-Free and Hybrid Electrocatalysts. *Chem. Asian J.* **2024**, e202400712. [CrossRef]
27. Xu, X.; Shao, Z.; Jiang, S. High-Entropy Materials for Water Electrolysis. *Energy Technol.* **2022**, *10*, 2200573.
28. Xiao, W.; Lei, W.; Gong, M.; Xin, H.L.; Wang, D. Recent Advances of Structurally Ordered Intermetallic Nanoparticles for Electrocatalysis. *ACS Catal.* **2018**, *8*, 3237–3256.
29. Sol, A.L.; Jeewon, B.; Jiwoo, L.; Ho, W.J. High-Entropy Nanomaterials for Advanced Electrocatalysis. *Small Sci.* **2023**, *3*, 2200109.
30. Wang, S.; Xu, B.; Huo, W.; Feng, H.; Zhou, X.; Fang, F.; Xie, Z.; Shang, J.K.; Jiang, J. Efficient FeCoNiCuPd thin-film electrocatalyst for alkaline oxygen and hydrogen evolution reactions. *Appl. Catal. B Environ.* **2022**, *313*, 121472. [CrossRef]
31. Lei, Y.; Zhang, L.; Xu, W.; Xiong, C.; Chen, W.; Xiang, X.; Zhang, B.; Shang, H. Carbon-supported high-entropy Co-Zn-Cd-Cu-Mn sulfide nanoarrays promise high-performance overall water splitting. *Nano Res.* **2022**, *15*, 6054–6061. [CrossRef]
32. Li, S.; Tong, L.K.; Peng, Z.; Zhang, B.; Fu, X. A novel high-entropy sulfide $(ZnCoMnFeAlMg)_9S_8$ as a low potential and long life electrocatalyst for overall water splitting in experiments and DFT analysis. *Green Chem.* **2023**, *26*, 384–395. [CrossRef]
33. Yang, P.; Sun, M.; Wang, J.; Li, J.; Yang, R.; Hao, Y.; Qi, L.; Yang, L.; Liu, X. High-entropy sulfurization enables efficient non-noble metal-based NiCoFeCuS electrocatalyst for alkaline oxygen evolution reaction. *Particuology* **2024**, *93*, 180–185. [CrossRef]
34. Feng, C.; Chen, M.; Zhou, Y.; Xie, Z.; Li, X.; Xiaokaiti, P.; Kansha, Y.; Abudula, A.; Guan, G. High-entropy NiFeCoV disulfides for enhanced alkaline water/seawater electrolysis. *J. Colloid Interface Sci.* **2023**, *645*, 724–734. [CrossRef] [PubMed]
35. Zhao, Y.; You, J.; Wang, Z.; Liu, G.; Huang, X.; Duan, M.; Zhang, H. High-entropy FeCoNiCuAlV sulfide as an efficient and reliable electrocatalyst for oxygen evolution reaction. *Int. J. Hydrogen Energy* **2024**, *70*, 599–605. [CrossRef]
36. Moradi, M.; Hasanvandian, F.; Bahadoran, A.; Shokri, A.; Zerangnasrabad, S.; Kakavandi, B. New high-entropy transition-metal sulfide nanoparticles for electrochemical oxygen evolution reaction. *Electrochimica Acta* **2022**, *436*, 141444. [CrossRef]
37. Cao, F.; Yang, X.; Shen, C.; Li, X.; Wang, J.; Qin, G.; Li, S.; Pang, X.; Li, G. Electrospinning synthesis of transition metal alloy nanoparticles encapsulated in nitrogen-doped carbon layers as an advanced bifunctional oxygen electrode. *J. Mater. Chem. A* **2020**, *8*, 7245–7252. [CrossRef]
38. Wang, R.; Huang, J.; Zhang, X.; Han, J.; Zhang, Z.; Gao, T.; Xu, L.; Liu, S.; Xu, P.; Song, B. Two-Dimensional High-Entropy Metal Phosphorus Trichalcogenides for Enhanced Hydrogen Evolution Reaction. *ACS Nano* **2022**, *16*, 3593–3603. [CrossRef]
39. Zhang, W.; Ma, X.; Zhong, C.; Ma, T.; Deng, Y.; Hu, W.; Han, X. Pyrite-type CoS2 Nanoparticles Supported on Nitrogen-Doped Graphene for Enhanced Water Splitting. *Front. Chem.* **2018**, *6*, 569.
40. Tan, Z.; Sharma, L.; Kakkar, R.; Meng, T.; Jiang, Y.; Cao, M. Arousing the Reactive Fe Sites in Pyrite (FeS_2) via Integration of Electronic Structure Reconfiguration and in Situ Electrochemical Topotactic Transformation for Highly Efficient Oxygen Evolution Reaction. *Inorg. Chem.* **2019**, *58*, 7615–7627. [CrossRef]
41. Fu, H.Q.; Zhang, L.; Wang, C.W.; Zheng, L.R.; Liu, P.F.; Yang, H.G. 1D/1D Hierarchical Nickel Sulfide/Phosphide Nanostructures for Electrocatalytic Water Oxidation. *ACS Energy Lett.* **2018**, *3*, 2021–2029. [CrossRef]
42. Zhao, X.; Li, X.; Yan, Y.; Xing, Y.; Lu, S.; Zhao, L.; Zhou, S.; Peng, Z.; Zeng, J. Electrical and structural engineering of cobalt selenide nanosheets by Mn modulation for efficient oxygen evolution. *Appl. Catal. B Environ.* **2018**, *236*, 569–575. [CrossRef]
43. Moradi, M.; Hasanvandian, F.; Afshar, M.G.; Larimi, A.; Khorasheh, F.; Niknam, E.; Setayesh, S.R. Incorporation of Fe in Mixed CoCu-Alkoxide Hollow Sphere for Enhancing the Electrochemical Water Oxidation Performance. *Mater. Today Chem.* **2021**, *22*, 100586.
44. Zhou, Y.; Yu, W.; Cao, Y.; Zhao, J.; Dong, B.; Ma, Y.; Wang, F.; Fan, R.; Zhou, Y.; Chai, Y. S-doped nickel-iron hydroxides synthesized by room-temperature electrochemical activation for efficient oxygen evolution. *Appl. Catal. B Environ.* **2021**, *292*, 120150. [CrossRef]
45. Gong, X.; Zhong, H.; Estudillo-Wong, L.A.; Alonso-Vante, N.; Feng, Y.; Li, D. Bifunctional oxygen electrode cobalt–nickel sulfides catalysts originated from intercalated LDH precursors. *J. Energy Chem.* **2022**, *74*, 376–386. [CrossRef]
46. Łukaszewski, M.; Soszko, M.; Czerwiński, A. Electrochemical Methods of Real Surface Area Determination of Noble Metal Electrodes-an Overview. *Int. J. Electrochem. Sci.* **2016**, *11*, 4442–4469.
47. Khaled, A.; Bilal, A.; Abdalla, O.; Mohammad, K.Q.; Abdel, M.R. Structural, electronic, and magnetic properties of X3Pt and XPt3 (X=Fe, Co, or Ni) alloys: Density functional theory and Monte Carlo simulation. *Phys. B Condens. Matter.* **2023**, *651*, 414615.

48. Kasatikov, S.; Fantin, A.; Manzoni, A.; Sakhonenkov, S.; Makarova, A.; Smirnov, D.; Filatova, E.; Schumacher, G. Chemical interaction and electronic structure in a compositionally complex alloy: A case study by means of X-ray absorption and X-ray photoelectron spectroscopy. *J. Alloys Compd.* **2020**, *857*, 157597. [CrossRef]
49. Kausar, A.; Eisa, M.H.; Aldaghri, O.; Ibnaouf, K.H.; Mimouni, A. Nanostructured Materials Derived from High Entropy Alloys–State-of-the-Art and Leading Technical Applications. *Results Phys.* **2024**, *62*, 107838.
50. Wang, Y.; Zhang, Y.; Xing, P.; Li, X.; Du, Q.; Fan, X.; Cai, Z.; Yin, R.; Yao, Y.; Gan, W. Self-Encapsulation of High-Entropy Alloy Nanoparticles inside Carbonized Wood for Highly Durable Electrocatalysis. *Adv. Mater.* **2024**, *36*, e2402391. [CrossRef]

Disclaimer/Publisher's Note: The statements, opinions and data contained in all publications are solely those of the individual author(s) and contributor(s) and not of MDPI and/or the editor(s). MDPI and/or the editor(s) disclaim responsibility for any injury to people or property resulting from any ideas, methods, instructions or products referred to in the content.